Particuology 100 (2025) 78–94

Contents lists available at ScienceDirect

Particuology

journal homepage: www.elsevier.com/locate/partic

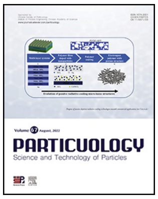

Modelling of heat transfer in moving granular assemblies with a focus on radiation using the discrete ordinate method: A DEM-CFD approach

Rezvan Abdi [*], Bo Jaeger, Enric Illana, Siegmar Wirtz, Martin Schiemann, Viktor Scherer

Institute of Energy Plant Technology, Ruhr-University Bochum, Universitätsstraße 150, 44780, Bochum, Germany

ARTICLE INFO

Article history:
Received 18 November 2024
Received in revised form
7 February 2025
Accepted 25 February 2025
Available online 14 March 2025

Keywords:
AVM
DOM radiation
DEM-CFD
OpenFOAM

ABSTRACT

Discrete Ordinates Method (DOM) is a model for thermal radiation exchange in opaque media. In this study, the DOM formulation is employed within the framework of the Discrete Element Method coupled with Computational Fluid Dynamics (DEM-CFD), thus including full radiative heat exchange among the phases involved. This is done by adjusting the absorption coefficient, emission coefficient, and net radiative heat flux of particles by incorporating local porosity into equations. A key objective is to represent radiation propagation for different packing densities in packed beds accurately.

The model is validated by comparing the results with available data from the literature for simulations with a P1 radiation model and corresponding experiments. The validation configuration is a heated box filled with spherical particles under vacuum conditions.

As an application example, the radiative heat exchange between an enclosure at high temperature and moving layers of spherical particles concurrently passed by a gas in crossflow is studied. Three packing densities (dilute, moderate, and dense) are examined to evaluate radiation penetration into the particle ensemble. Convective and contact heat transfer are also considered. The DEM-CFD coupling is a non-resolved approach, where the influence of particles on the flow field is accounted for by momentum and energy source terms together with a porosity field (Averaged Volume Method (AVM)).

Effect of convective, conductive and radiative heat transfer is analysed based on the evolution of incident radiation flux, spatial distributions of particle surface and fluid temperatures, and particle temperature histograms. It becomes obvious that radiation dominates the system, and that packing density defines the penetration depth of radiation. Conduction mainly leads to a smoothening of particle temperature distribution in the system.

1. Introduction

For many industrial applications, including rotary drums (Scherer et al., 2016), grate firing systems (Silva et al., 2021), shaft kilns for lime (Krause et al., 2017) and spinel production (Spijker et al., 2023), or blast furnaces (Peters et al., 2018), the study of moving granular assemblies in close heat exchange with their surroundings is crucial. Particulate systems can be classified according to the concentration of solids they handle: dilute systems, like pneumatic conveying; moderately dense systems, such as fluidized beds (Peng et al., 2020) and dense systems, including rotary drums and moving packed beds. Consequently, each type of system requires an adapted modelling approach to capture the dynamics and heat transfer characteristics effectively. In many technical applications, granular material is also subject to simultaneous fluid flow. Fluid flow is frequently employed to transport particles, provide heat, facilitate cooling, or act as a reactive component within a particular process. Radiation, convection and solid-conduction can occur as heat transfer phenomena. Particularly, the presence of radiation adds to the complexity of the multiphysics problem (Jaeger et al., 2023).

---

[*] Corresponding author.
E-mail address: Abdi@leat.ruhr-uni-bochum.de (R. Abdi).

https://doi.org/10.1016/j.partic.2025.02.024
1674-2001/

Nomenclature

a	Absorption coefficient, m^{-1}
A	Area, m^2
$C_{p,p}$	Particle specific heat capacity, J kg^{-1} K^{-1}
E	Cell emission, W m^{-3}
G	Incident radiation, W m^{-2}
g	Acceleration due to gravity, m s^{-2}
h_e	Enthalpy, J
htc	Heat transfer coefficient, W m^{-2} K^{-1}
I	Radiation intensity, W m^{-2} sr^{-1}
I_0	Boundary radiation intensity, W m^{-2} sr^{-1}
k	Thermal conductivity, W m^{-1} K^{-1}
$\dot{m}_{spheres}$	Particle mass flux, kg s^{-1}
n	Unit normal vector
N_{shell}	Number of shells
N	Number of particles
Nu	Nusselt number
N_θ, N_φ	Number of polar/azimuthal angles per quadrant
Pr	Prandtl number
P	Pressure (relative to atmospheric pressure), Pa
P_{rgh}	Gauge pressure, Pa
$\dot{Q}$	Heat rate, J s^{-1}
Re	Reynolds number
R	Radius of particle, m
r '	Radial coordinate, m
r	Ray position vector, m
s	Ray direction vector
S_m	Mass source term, kg m^{-3} s^{-1}
S_h	Convective heat transfer source term, W m^{-3}
$S_{h,m}$	Source term considering variations in sensible enthalpy resulting from mass sources, W m^{-3}
S_{rad}	Radiation sources, W m^{-3}
S_{react}	Sources considering energy changes arising from reactions, W m^{-3}
S_{sf}	Momentum source/sink, N m^{-3}
S_ϕ	Scattering source term, W m^{-3}
t	Time, s
$t_{residence}$	Residence time, s
T	Temperature, K
$T_{g,inlet}$	Gas temperature at the inlet, K
$\overline{T}_{p,outlet}$	Average particle temperatures at outlet of domain, K
V	Cell volume, m^3
v	Velocity, m s^{-1}
$v_{spheres}$	Spheres velocity, m s^{-1}
$v_{g,inlet}$	Gas velocity at the inlet, m s^{-1}
x	Distance, m
Y	Young's modulus, Pa
Greek letters	
α_{eff}	Effective thermal diffusivity, m^2 s^{-1}
ε	Emissivity
ν_p	Particle Poisson's ratio
ρ	Density, kg m^{-3}
σ	Stefan-Boltzmann constant, W m^{-2} K^{-4}
σ_s	Scattering coefficient, m^{-1}
τ	Stress tensor, Pa
ϕ	Porosity
ϕ'_{CV}	Averaged fluid properties, variable
$\phi'_{element}$	Averaged fluid properties of the element, variable
Ω	Angular space, sr
ω'_{CV}	Weighting factor
ω_i	Discrete solid angle, sr
Abbreviations	
AVM	Averaged volume method
CFD	Computational fluid dynamics
CV	Control volume
DOM	Discrete ordinates method
DEM	Discrete element method
RTE	Radiative transfer equation
Subscripts	
cell	Cell
conv	Convection
CV	Control volume
D − P	Enclosure domain and the particles
element	Of the element
face	Face
g	Gas
in	Incoming
net	Net value
out	Outgoing
p	Particle
P − P	Particle to particle
Proj	Projected
rad	Radiation
t	Total
w	Wall

(continued on next page)

(continued)

Peng et al. (Peng et al., 2020) state “Despite the significant progress achieved in the measuring techniques of heat transfer, e.g…, it proves extremely challenging (if not impossible) to fully understand the heat transfer characteristics of particulate systems via the experimental approach alone”. As a result, numerical approaches like DEM-CFD have gained popularity. An appropriate model should contain all the heat transfer mechanisms mentioned above. A comprehensive overview on current approaches for convective, conductive and radiative heat transfer in DEM-CFD can be found in (Peng et al., 2020).

In DEM-CFD with a large number of particles, the effect of the bulk of particles in the Eulerian CFD framework is described via a porous medium approximation with a time-resolved porosity distribution derived from DEM. This is commonly denoted as unresolved DEM-CFD or “Average Volume Method” (AVM). The method is also used in the present study. This porosity-based technique avoids continuous remeshing as for body conformal CFD meshes, and is superior in terms of computing times compared to immersed boundary methods. AVM proves advantageous, notably in simulating device-scale scenarios where individual particle dimensions are considerably smaller than the CFD control volumes (CVs). Hence, it allows for computationally efficient simulations in reasonable times. Within the AVM framework, multiple particles are enclosed within a CFD control volume, retaining solid-fluid interactions at their interface within the subgrid. However, because the fluid flow lacks information about the particles' detailed geometry (due to the coarse mesh resolution), inaccuracies in the flow field may occur. One inherent outcome of this porosity-based method is the necessity to characterize the influence of actual particle shape on momentum, heat, and mass transfer between particles and the fluid by utilizing correlations (drag, Nusselt, Sherwood correlations). These correlations must be calibrated for actual particle shape to ensure accurate results (Jaeger et al., 2021, 2023).

In high-temperature particulate systems, radiative heat transfer may occur among fluid, walls and particles. For densely packed beds, gas radiation is often neglected due to the short optical path length. The available models for radiation are generally classified into two categories: discrete approaches and continuum approaches.

In the discrete approach, particles are treated as individual entities that interact through radiative heat exchange at their surfaces. The heat transfer between these surface elements is influenced by various factors, including their temperatures, surface properties, size, relative orientation, and separation distance. The geometric variables are summarized in a single parameter, known as the view factor (Peng et al., 2020). A view factor quantifies the proportion of energy emitted by one particle that reaches the surface of another particle (Mačak et al., 2023). Calculating the view factor between two particles can be difficult. Very often analytical solutions do not exist, even for simple particle geometries. Therefore, highly simplified assumptions are often made for the view factor, such as assuming that it can be determined by the surface area of neighbouring particles. These highly simplified assumptions are very common in current DEM simulations (Peng et al., 2020; Peters, 2002; Peters et al., 2018, 2019; Spijker et al., 2023; Wu et al., 2020). Although not highly accurate, this approach has the advantage that it can also be applied to moving particle systems with limited computational effort. Such an approach does not allow to consider shadowing effects by other particles. Forgber and Radl (2018) introduced a method for calculating view factors that considers shadowing for a monodisperse bed of spherical particles. They stated that the method can only be applied for small-scale systems due to the computational effort. In (Tausendschön et al., 2023), they extended their method to polydisperse granular assemblies of spherical particles using machine learning methods, significantly reducing computational effort. Handling complex-shaped particles currently appears to be unfeasible due to the increased complexity and computational effort required to account for the view factors of all the particle faces and re-computation of the view factors when particles move.

Continuum-based models are an alternative. They consider the compound of particles and the enclosing gas as a two-phase continuous medium. These models are formulated based on the radiative transfer equation (RTE) for spatially varying absorbing, scattering and emitting continuous media (Jaeger et al., 2023). The presence of particles and their spatial distribution domain is accounted for by effective absorption and emission properties in the respective control volumes (CFD-cells). In the AVM approach used here, where typically more than one particle is contained within a cell, the continuum model cannot account for shadowing among individual particles which are in one fluid cell. Instead, it considers “particle layer” shadowing among neighbouring fluid cells. This “layer shadowing” allows to predict the net penetration depth of radiation in packed beds, as will be demonstrated in the results section.

In its most general form, the RTE is a function of wavelength, two angular coordinates (azimuthal and zenith angle), and three spatial coordinates. For simplicity, the wavelength dependency is not considered here. There are different strategies for handling the angular dependency. The Discrete Ordinates Method (DOM) (Chandrasekhar, 1950; Modest, 2013), and the Spherical Harmonics Approximation (Mačak et al., 2023) are two well-known approaches. DOM involves additional domain discretization along prescribed spatial directions (solid angles). The most common Spherical Harmonics Approximation is the P1-approximation but, this model is accurate only for isotropic radiative fields (Mačak et al., 2023). In addition, variations in radiative properties affect the P1 model's accuracy (Dombrovskii, 1997; Dombrovsky, 2010; Modest, 2013; Viskanta & Mengüç, 1987). These non-uniform properties are prevalent in many gas-particle systems, like grate firing systems or fluidized beds, where time varying spatial distributions in the concentration of particles are common (Mačak et al., 2023). Furthermore, the equation of radiative heat transfer predicts temperature jumps at points of discontinuity (Heaslet & Warming, 1965). These temperature jumps cannot be resolved by the P1 model, as it is a first-order approximation. In a recent study using the P1 model (Mačak et al., 2023), unphysical oscillations in heat flux were observed near areas with sharp gradients in the solid fraction field.

For the present contribution, the DOM method was selected, as it is especially suitable for situations where radiation shows directional variability. This method involves dividing the radiation field into a set of ordinate directions, $\overrightarrow{s}$, in which the radiation propagates in the medium. Each direction within the global Cartesian system remains fixed. Because of this structural change, the RTE is now a transfer equation for radiation intensity, $I_{(\overrightarrow{s}, \overrightarrow{r})}$. The radiative intensity field is computed by solving the RTE for each direction. Each of these spatial directions, $\overrightarrow{s}$, is connected to discrete solid angles, ω_i. The angular space 4π is divided into N_θ polar angles and N_φ azimuthal angles per quadrant. A quadrant refers to one of the four equal parts into which three-dimensional space can be divided by the three coordinate planes. These coordinate planes are the x-axis, y-axis, and z-axis in Cartesian coordinates. Consequently, each quadrant is subdivided into $N_\theta N_\varphi$ solid angles. This results in a total of 4 $N_\theta N_\varphi$ directions for three-dimensional analysis (Modest, 2013).

In a recent study (Tavakkol et al., 2023), significant attention was focused on DOM for densely packed bed configurations. It specifically focuses on the particle layer shadowing phenomenon. This involved developing and integrating modified absorption/emission coefficients within OpenFOAM to model radiative transfer. A crucial aspect of this study was the introduction of a high (but not generally applicable) absorption coefficient to absorb radiation completely in CVs densely occupied by particles. In the current work, a modified approach that circumvents complete absorption is suggested, the details of the mathematical formulation will be presented in section 2.

In this study, the interaction between a heated wall, moving particle layers, and a crossing gaseous fluid (air), is considered while focusing on three situations: dilute (porosity $(\varnothing) = 93\%$), moderate ($\varnothing = 66.5\%$), and densely packed particle layers ($\varnothing = 34.5\%$). The dilute, moderate, and dense cases consist of 540, 2560, and 5000 randomly distributed spheres whose solid mass flow is kept constant (i.e., they have different solid velocities and residence time). These particles move along a fixed path inside a rectangular domain, gradually heating as they progress towards the exit. The temperature of the particles increases due to simultaneous thermal radiation exchanged with a high-temperature ceiling wall and convective heat transfer caused by the passing fluid.

The novelty of the present study is the analysis of the interplay of convective, conductive (contact-heat transfer between particles), and radiative heat transfer, specifically in a moving packed system ranging from dilute to densely packed configurations within a unified computational framework. This study aims to adjust absorption and emission coefficients within systems composed of heat-absorbing spherical particles for all packing densities, such that radiative heat to/from the particles is correctly distributed into the fluid cells. Hence, it improves the applicability of the DOM model. Furthermore, if just the net radiation shadowing effect of areas of different packing densities is of interest, the DOM model used in this study may avoid the need for a discrete (particle-particle) radiation model.

The model has been implemented into an in-house DEM software, currently under development in the collaborative research center Bulk-Reaction, and the open-source software OpenFOAM for CFD analysis.

The article is structured as follows: in section 2, the mathematical formulation of the governing equations is presented; in section 3, the modelling approach is validated based on packed bed experiments in vacuum and by comparing it to the corresponding simulations of the same setup with the P1 model; section 4 describes the test case, a system of moving particle with gas flow, section 5 presents and discusses the results and section 6 summarizes the findings.

2. Mathematical formulation

2.1. Fluid phase

This study assumes that the fluid flow is laminar. The governing equations for fluid flowing through a porous medium consist of mass conservation (Eq. (1)), momentum conservation (Eq. (2)), and energy conservation (Eq. (3)). To account for the existence of particles, local porosity $\varnothing$ and particle source terms have been included.

$$\frac{\partial(\varnothing\rho_g)}{\partial t}+\vec{\nabla}\cdot(\varnothing\rho_g\vec{v})=S_m \tag{1}$$

$$\frac{\partial(\varnothing\rho_g\vec{v})}{\partial t}+(\vec{\nabla}\cdot(\varnothing\rho_g\vec{v})\times)\cdot\vec{v}=-\varnothing\vec{\nabla}P_{rgh}-\varnothing\vec{\nabla}\rho_g\vec{g}\vec{x}+\vec{\nabla}\cdot(\varnothing\vec{\tau})+\vec{S}_{sf} \tag{2}$$

$$\frac{\partial(\varnothing\rho_g h_e)}{\partial t}+\vec{\nabla}\cdot(\varnothing\rho_g\vec{v}h_e)-\vec{\nabla}\cdot\left(\varnothing\alpha_{eff}\nabla h_e\right)=S_{h,m}+S_h+S_{rad}+S_{react} \tag{3}$$

The variables gauge pressure, gas density, velocity, and time are represented by P_{rgh}, ρ_g, $\vec{v}$, and t, respectively. Additionally, h_e, α_{eff}, τ, and $\varnothing$ correspond to enthalpy, the effective thermal gas diffusivity, stress tensor, and porosity, respectively. $\vec{S}_{sf}$ is a momentum source/sink and deals with the presence of unresolved (AVM) particles. It captures the dynamic forces between the fluid and these particles and is modelled here by the Ergun equation (Ergun, 1952). The mass source is denoted by S_m and this study assumes that it is zero (particles do not react).

The first term on the left side of Eq. (3) represents the change in enthalpy within a control volume over time. The second term accounts for variations in enthalpy due to convective heat transfer. The third term addresses changes attributed to conductive heat transfer.

On the right side of Eq. (3), $S_{h,m}$, accounts for variations in sensible enthalpy resulting from mass sources. Thermal energy coupling involves convective heat transfer between the fluid and the solid. This convective heat transfer is incorporated into the energy equation (Eq. (3)) as a source term (S_h). S_{rad} denotes the contribution from gas radiation which is assumed to be zero in this study. S_{react} accounts for energy sources arising from reactions, which is also assumed to be zero. It's worth noting that in this study, radiation from surrounding walls initially interacts with the particles (Eq. (6)), heating them up, and then subsequently influences the fluid part via the convective source term, S_h.

The AVM operates on the premise that any particle existing within the flow domain behaves as a Lagrangian entity that interacts with one or several CVs. An arbitrary fluid property ϕ'_{CV} is interpolated onto an element by the following formulation:

$$\phi'_{element}=\sum\omega'_{CV}\phi'_{CV} \tag{4}$$

$$\sum\omega'_{CV}=1 \tag{5}$$

The weights, ω'_{CV}, which depend on a Gaussian kernel function (Wang et al., 2019), are CV-related and they are only applicable when a particle has contact with several CVs. Moreover, the distribution of source terms, influenced by these averaged properties and the particle volume, mirrors the distribution across the respective CVs (Illana Mahiques et al., 2023).

2.2. Solid phase

For an individual particle, the energy conservation equation in its differential form is:

$$\rho_p c_{p,p}\frac{\partial T_p}{\partial t}=\frac{1}{r'^2}\frac{\partial}{\partial r'}\left(r'^2 k_p\frac{\partial T_p}{\partial r'}\right)+\dot{Q}_{conv}+\dot{Q}_{net\ rad\ D-P}+\dot{Q}_{contact\ P-P} \tag{6}$$

where r' is radial coordinate. An implicit numerical scheme was used to solve Eq. (6), with the tridiagonal matrix algorithm (TDMA). In this work, particles are spherical and discretized in shell-volumes ($N_{shell}=40$), so Eq. (6) is effectively a 1D-Transport equation. The meaning of each term is as follows:

The first term on the left side ($\rho_p c_{p,p}\frac{\partial T_p}{\partial t}$) represents the variation of temperature inside each particle over time. $\frac{1}{r'^2}\frac{\partial}{\partial r'}\left(r'^2 k_p\frac{\partial T_p}{\partial r'}\right)$ represents the conductive heat transfer in radial direction inside a particle. $\dot{Q}_{conv}$ denotes the convective heat transfer between the fluid and the particle. $\dot{Q}_{net\ rad\ D-P}$ represents the net radiation exchange between the entire enclosure domain and the particle.

$\dot{Q}_{contact\ P-P}$ represents the conductive heat transfer exchanged with another particle (or wall). This term is modelled by the approach of McCarthy and Vargas (Vargas & McCarthy, 2001, 2002) and we refer to their publication for details. It should be noted that the term $\dot{Q}_{contact\ P-P}$ includes two phenomena: the direct heat transfer through the contact point of the two solids, calculated based on Hertzian contact theory, and the heat transferred trough the gas layer in the vicinity of the contact point, which is dependent on thickness of the gas layer between the two solids.

To obtain the convective heat exchange between particles and the surrounding fluid flow on the DEM side, $\dot{Q}_{conv}$ in Eq. (6), Newton's law is used:

$$\dot{Q}_{conv}=A_p\ htc\ (T_g-T_p) \tag{7}$$

where A_p ($=4\pi R^2$) is the particles surface area and htc is the heat transfer coefficient which is computed from the Ranz-Marshall Nusselt number correlation (Ranz & Marshall, 1952):

$$Nu=2+0.6\sqrt{Re}\sqrt[3]{Pr} \tag{8}$$

$$htc=0.5\ Nu\ k_g/R \tag{9}$$

where k_g is the gas thermal conductivity, R is radius of particles, Re is the Reynolds number and Pr is the Prandtl number. Since this correlation applies to a single particle, we applied Gnielinski's correction (Gnielinski, 1980) to account for the influence of particle packing:

$$Nu_{i,p}=(1+1.5\cdot(1-\varnothing))\cdot Nu_{i,p} \tag{10}$$

To obtain $\dot{Q}_{net\ rad\ D-P}$ in Eq. (6), another set of equations needs to be solved, as discussed in the following section.

2.3. Radiation modelling

Both the Eulerian and Lagrangian computational domains require the simultaneous consideration of radiation. First, the equations utilized in the Eulerian frame are explained.

The total radiative intensity in a fluid cell is represented by the incident radiation G [W/m^2]:

$$G_{\vec{r}}=\int_0^{4\pi}I_{(\vec{s},\vec{r})}d\Omega\approx\sum_i I_{(\vec{s},\vec{r})}\cdot\omega_i \tag{11}$$

where Ω is the angular space, ω_i represents the discrete solid angle corresponding to the direction i. The term $I_{(\vec{s}, \vec{r})}$ represents the radiation intensity [W/(m^2 sr)] in the direction denoted by $\vec{s}$ and at position $\vec{r}$. This value of G is later interpolated onto the particle positions, where it is referred to as G_{CV}.

It is clear from Eq. (11) that determining $I_{(\vec{s}, \vec{r})}$ is necessary for calculating G. To determine $I_{(\vec{s}, \vec{r})}$, the DOM solves a pre-defined number of RTEs. Note that for all radiation simulations in this study, a discretization of 3 azimuthal angles (N_φ) and 4 polar angles (N_θ) for each quadrant of the angular space was selected, resulting in a total of 48 RTEs to be solved.

The RTE, Eq. (12), provides a description of the propagation of radiation along a direction $\vec{s}$ within a medium. It considers absorption, emission, and scattering of radiation within the medium along the ray's path (see Fig. 1).

$$\nabla \cdot I_{(\vec{s}, \vec{r})} \cdot \vec{s} = -(a_t + \sigma_s) I_{(\vec{s}, \vec{r})} + a_g \frac{\sigma T^4}{\pi} + S_\varnothing + E_t \tag{12}$$

The left side of the equation indicates the spatial variation of radiation intensity within the medium. The first term on the right side of the equation describes the local change of thermal radiation due to absorption and scattering. The second term denotes changes due to gas emission, where σ denotes the Stefan-Boltzmann constant. $S_\varnothing$ signifies the scattering phase function and E_t represents total cell emission in units of W/m^3. T denotes the local gas temperature of fluid cells, a_t represents the total absorption coefficient, and σ_s signifies a scattering coefficient. The total absorption (a_t) is assumed to be the sum of gas absorption (a_g) and particle absorption (a_p). The total cell emission (E_t) can be written as the sum of gas emission (E_g) and particle emission (E_p). Hence, Eq. (12) can be written as:

$$(\nabla \cdot I)_{(\vec{s}, \vec{r})} \cdot \vec{s} = -\left(a_g + a_p + \sigma_s\right) I_{(\vec{s}, \vec{r})} + a_g \frac{\sigma T^4}{\pi} + S_\varnothing + \left(E_g + E_p\right) \tag{13}$$

By assuming $a_g = \sigma_s = S_\varnothing = E_g = 0$, Eq. (13) can be summarized to:

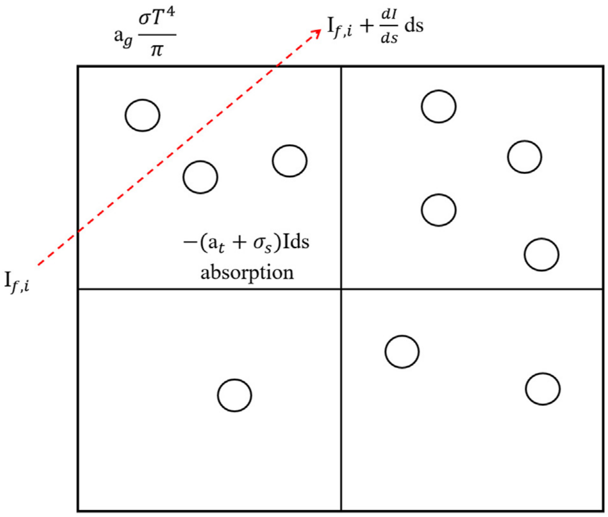

Fig. 1. Consideration of particle presence by adjusting the absorption and emission terms of the Radiative Transfer Equation (RTE). The squares represent the CFD cells.

$$(\nabla \cdot I)_{(\vec{s}, \vec{r})} \cdot \vec{s} = -a_p\, I_{(\vec{s}, \vec{r})} + \frac{E_p}{4\pi} \tag{14}$$

In Eq. (14), it is further assumed that the particles are diffuse emitters and that their emitted radiation equally contributes to the intensity in all spatial directions. Hence, the particle emission E_p is divided by 4π.

The radiation balance for a single CFD control volume leads to the discretized form of the RTE:

$$\sum_{i}^{N_{ray}} \sum\nolimits_{face} I_{face,i} \vec{S}_i \vec{A}_{face} = -a_p\, \omega_i I_{cell,i} + \frac{E_p}{4\pi}\omega_i \tag{15}$$

where $\vec{S}_i = \vec{s}_i \omega_i$. From Eq. (15), it becomes evident that by adjusting a_p and E_p, the influence of particles onto radiation passing through the cell is incorporated. In this work, we adjust a_p and E_p depending on local porosities and number of particles. By doing so, different packing densities of particles assemblies can be considered in the simulation or locally time varying porosities/particle numbers may be accounted for. E_p in the Eulerian computational domain is equal to:

$$E_p = \frac{1}{V}\varnothing \sum_{i=1}^{N} \varepsilon_p A_{p,i} \sigma T_{p,i}^4 \tag{16}$$

where $A_{p,i} = 4\pi R^2$ is the surface area of a particle i, ε_p is the emissivity of the particle, V is the CFD cell volume and N is the number of particles in CFD cell. Consequently, E_p is zero in cells not occupied by any particles. The absorption coefficient a_p [m^{-1}] in Eq. (15) can be obtained using:

$$a_p = \frac{1}{V}\varnothing \sum_{i=1}^{N} \varepsilon_p A_{Proj,i} \tag{17}$$

In this equation, the projected area of particles ($A_{Proj,i} = \pi\ R^2$) is used as effective surface for absorbing radiation. As the cell absorption depends on the number of particles, this also means that shadowing effects are accounted for, at least among CFD cells. With increasing particle number, a_p becomes larger and more radiation is absorbed in the cell.

One of the main objectives of this paper, as discussed previously, is to adjust absorption a_p and emission E_p and the net radiative heat flux of particles within the system, $\dot{Q}_{net\ rad\ D-P}$, while maintaining a balance between them. To achieve this balance, it is necessary that the emission and absorption terms inserted in the RTEs are reflected in the heat balance $\dot{Q}_{net\ rad\ D-P}$ for a Lagrangian particle. The radiative balance between absorption and emission is as follows:

$$\dot{Q}_{net\,rad.\,D-P} = \dot{Q}_{absorbed\,rad.\,p.} - \dot{Q}_{emmited\,rad.\,p.} = \varepsilon_p \varnothing A_p \left(\frac{G_{CV}}{4} - \sigma T_p^4\right) \tag{18}$$

The value G_{CV} was already attuned by the presence of the particles through the inclusion of a_p and E_p in the RTEs, as described above. Eq. (18) assumes that the particle experiences a spatially homogenous radiation field.

All walls of the enclosure are also assumed to be gray and diffuse emitters. Incoming radiation $\dot{q}_{Rad,in}$ [W/m^2] to the boundary of the enclosure from all directions is determined by evaluating if $\vec{s} \cdot \vec{n} > 0$ is met, with $\vec{n}$ being the boundaries normal vector, pointing outside the domain.

$$\dot{q}_{Rad,in} = \int_0^{4\pi} I_s \cdot \overrightarrow{s} \cdot \overrightarrow{n}\, d\Omega \xrightarrow{\text{the discretized form}} \dot{q}_{Rad,in} = \sum\nolimits_i I_s \cdot \overrightarrow{s} \cdot \overrightarrow{n} \cdot \omega_i \tag{19}$$

The outgoing radiation for all directions where the condition $\overrightarrow{s} \cdot \overrightarrow{n} < 0$ is met is given by:

$$\dot{q}_{Rad,out} = (1 - \varepsilon_W)\dot{q}_{Rad,in} + \varepsilon_W \sigma T_W^4 \tag{20}$$

where T_W and ε_W are the temperature and emissivity of the wall. From Eq. (20), the emitted radiative Intensity I_0 is calculated assuming that radiation is emitted diffusively into the hemisphere above the wall:

$$I_0 = \dot{q}_{Rad,out} \Big/ \pi \tag{21}$$

3. Validation

The DOM model combined with solid contact heat transfer is validated using both experimental and numerical data for a pebble bed under vacuum conditions. The geometry used for the DOM simulation is based on the experiments conducted by De Beer (De Beer, 2014), as shown in Fig. 2. The setup is a cubical box with dimensions of 0.42 × 0.42× 0.42 m^3. It contains 332 spherical graphite pebbles with radius of 0.03 m arranged between a heated (left) and a cooled (right) wall. The box has been filled by a DEM simulation with the particles dropping from the top. The heated and cooled wall are also made of graphite and maintained at isothermal conditions. The other walls (top, bottom, rear and front) have pre-defined temperatures as listed below. The numerical data used for comparison are based on the P1 radiation model of Mačak et al. (Mačak et al., 2023). Two tests were conducted: the first analysed heat transfer with radiation only, while the second involved a combined analysis of radiation and conduction. Each test considered two different temperature values at the heated and cooled walls:

- 400 °C of the left wall and 59.39 °C of the right wall
- 800 °C of the left wall and 163.35 °C of the right wall

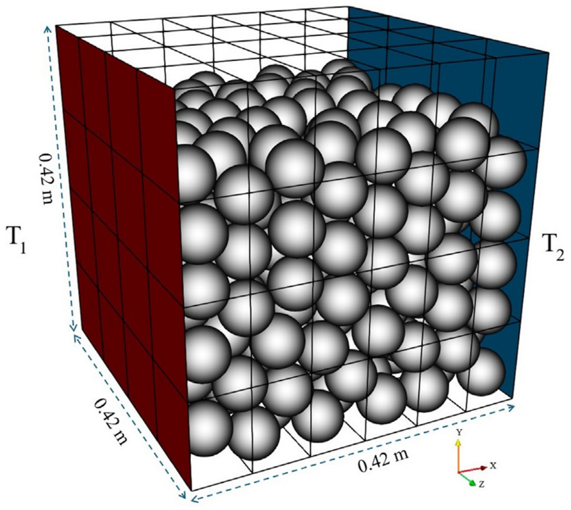

Fig. 2. Simulation domain for the pebble bed under vacuum conditions.

In addition, based on fitting the experimental temperature data from De Beer (De Beer, 2014), two temperature profiles are considered at the top, bottom, rear and front wall with x being the spatial coordinate.

$$400\ ^\circ\mathrm{C} : T\,(x)[\mathrm{K}] = -598.19\,x^2 - 484.58\,x + 697.66$$

$$800\ ^\circ\mathrm{C} : T\,(x)[\mathrm{K}] = -1757.6\,x^2 - 479.12\,x + 1077.1$$

The thermal conductivity k of the graphite (for particles, heated and cooled walls) is significantly dependent on temperature, and varies with temperature according to the below function provided by fitting the corresponding data from De Beer (De Beer, 2014):

$$k\,(T)\left[\frac{\mathrm{W}}{\mathrm{m}\cdot\mathrm{K}}\right] = \left(-6\times10^{-8}\right)T^3 + 0.0002\,T^2 - 0.3554\,T + 240.047$$

It is worth noting that the thermal conductivity of graphite (e.g., 92 W/m·K at 400 °C (De Beer, 2014)) is much larger than that of the other side walls, which are made from refractory material with a thermal conductivity of 0.2 W/m·K. Additional simulation parameters are detailed in Table 1.

Fig. 3(a) depicts the steady-state temperatures of each individual particle along the x-direction considering only radiative heat transfer for the 400 °C (upper left) and 800 °C (lower left) cases, respectively. The DOM results show good agreement with the P1 model.

When conduction is included in the heat transfer analysis, compared to the radiation solution only, the particle temperature is slightly increased near the heated wall and decreased significantly close to the cooled wall. Fig. 3(b) illustrates this effect for 400 °C (upper right) and 800 °C (lower right) cases. In both instances, the numerical results are also in good agreement with the experimental data. The comparison with the experimental data highlights the accuracy of the present approach in capturing the combined effects of conduction and radiation. Based on this validation, the next section will examine a more complex setup of moving particles, and it will also include the effect of convection.

Note that accurate description of convective heat transfer has been validated in our previous studies (Rickelt et al., 2013; Sudbrock et al., 2015).

4. Test case: numerical setup, geometry and boundary conditions

As the motivation of the current paper is the analysis of the interplay of convective, conductive, and radiative heat transfer in moving packed beds of spatially varying packing density, a test case

Table 1
Simulation parameter used for validation case.

Parameter	Symbol	Unit	Value
Simulation time step	Δt	[s]	0.05
Emissivity of particles	ε_p	[−]	0.8
Emissivity of heated/cooled wall	ε_w	[−]	0.8
Emissivity of top, bottom, rear and front walls	ε_w	[−]	0.67
Absorption coefficient of top, bottom, rear and front walls	a_w	[m^{-1}]	0.67
Absorption coefficient of heated/cooled walls	a_w	[m^{-1}]	0.8
Absorption coefficient of particles	a_p	[m^{-1}]	Eq. (17)
Heat capacity of particles and all walls	c_p	[J/(kg·K)]	710
Young's modulus of particles and all walls	Y	[GPa]	11
Density of particles and all walls	ρ	[kg/m^3]	1650
Side walls thermal conductivity	k	[W/(m·K)]	0.20

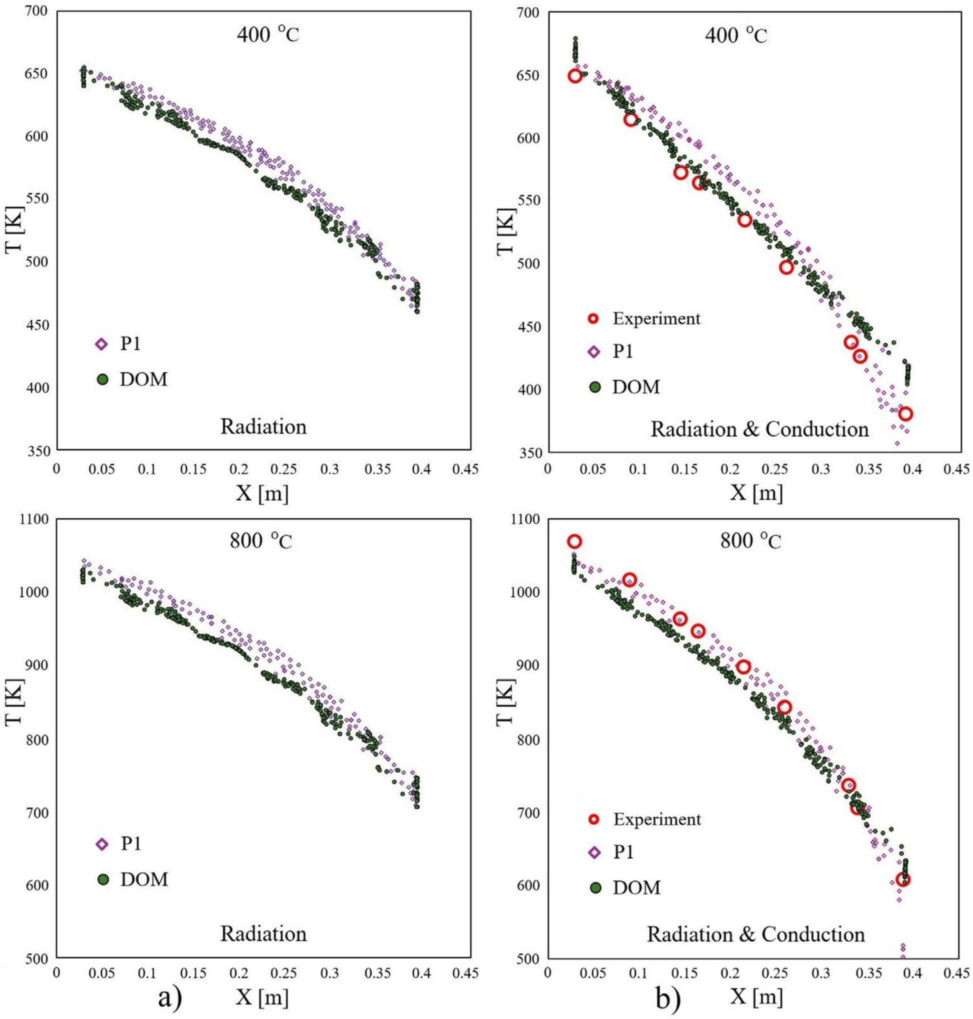

Fig. 3. Temperature distribution along the x-direction in the cubic domain presented in Fig. 2 under vacuum conditions.

has been setup that allows for such an analysis. This test case is depicted in Figs. 4–6.

A box with dimensions of 0.4 × 0.3 × 0.1 m^3 is used (Fig. 4). The domain is meshed by 6200 hexahedral elements. The upper part is meshed with smaller elements, and the polyhedral elements are located at the intersection of the small and large cells. The gas flow enters the domain from the bottom surface and exits through a small outlet with the dimension of 0.02 × 0.02 m^2, located at the top of the right boundary of the box (red area shown in Fig. 4). The particles are located in the blue region shown in Fig. 4. The particle region has a height of 0.1 m, and the particle flow occurs through the left boundary whose dimensions are 0.1 m × 0.1 m. The particles exit through the right outlet boundary. The particle region is positioned within a larger enclosure, leaving a free space both above and below the particle layer. Specifically, the lower layer of particles is positioned 0.1 m above the bottom boundary of the box, and the top layer of particles is 0.1 m below the top wall. Three distinct arrangements of spheres are used, as shown in Fig. 5. The first is a dilute case composed of 540 spheres, followed by a moderate case with 2560 spheres, and a dense case with 5000 spheres.

The packing porosities within the sphere zone (not the entire box) are 93 %, 66.5 %, and 34.5 % for the cases with 540, 2560, and 5000 spheres, respectively (see Table 1). It should be emphasized that these porosities are mean values; however, in the fluid equations, the local porosity in each fluid cell is used.

The cases are generated as follows: First, 5000 spheres are randomly distributed in the domain by dropping the spheres from the top by a DEM simulation. Next, nearly half of the spheres are arbitrarily eliminated to create a moderate case, and lastly, nearly 2000 more spheres are arbitrarily removed to reach the dilute case. There is an average of 10, 5.12, 1.08 spheres in each fluid cell for the dense, moderate and dilute cases, respectively.

For each case, a constant velocity in the x-direction is imposed to all the particles (i.e., the particles follow a prescribed motion and the mechanical part of DEM describing particle motion is not further solved, only the thermal part of the DEM code). The particle velocities differ across the three cases (see Table 2). However, all cases maintain the same mass flux of particles. The particle mass flux is 3.665 g/s, resulting in the entry of 10 particles per second into the domain. The time required for one particle to move from the left to the right of the box, $t_{residence}$, is shown in Table 2.

The passing fluid is assumed to be air with a thermal conductivity of 0.04 W/(m·K). The assumed material properties for the solid, considered to be wood, are as follows: $\rho_p = 700$ kg/m^3 is the density of the particles and $c_{p,p} = 1500$ J/(kg·K) is the specific heat capacity of the particles, $k_p = 0.19$ W/(m·K) is the thermal conductivity of the particles and T_p is the surface (the most outer shell)

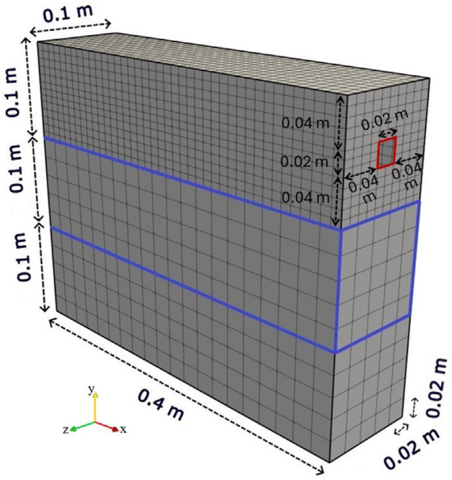

Fig. 4. The meshed domain.

temperature of the particles. All particles have a radius of 5 mm, with an emissivity ε_p of 0.85. Table 3 displays all the simulation parameters.

The boundary conditions are depicted in Fig. 6. The air (23 mass % O_2 and 77 mass % N_2) enters the domain from the bottom with the velocity of 0.3 m/s and exits the domain at the top right. The inlet temperature of the passing gas, $T_{g,inlet}$, is fixed at 1373.15 K. The particles enter the domain from the left at 298.15 K and exit the domain at the right side. The outlet has a zero-gradient boundary condition for velocity and temperature. The pressure P at the outlet is zero relative to atmospheric pressure. The velocity of the fluid at all walls is zero (no slip condition). Furthermore, all walls are adiabatic.

A fixed temperature of $T_{rad} = 2573.15$ K is defined for the top wall, while the remaining walls are maintained at $T_{rad} = 298.15$ K.

Four different scenarios are simulated for each packing density.

Scenario I: Exclusively considers radiation effects from the top wall. Convective heat transfer and thus conductive exchange among particles are neglected.

Scenario II: Focuses solely on convective heat transfer between the fluid and particles.

Scenario III: Enhances scenario II by incorporating conduction among spheres.

Scenario IV: Convection, conduction, and radiation are all active.

5. Results and discussion

The results of this section demonstrate the effects of three distinct heat transfer mechanisms—convection, conduction, and radiation—in a system of spherical particles exhibiting three different packing densities (540, 2560, and 5000 particles). The analysis is based on the evolution of particle surface temperatures, fluid temperature distributions, particle temperature histograms and incident radiative heat fluxes. All results correspond to the end of several particle residence times for each case in order to reach steady-state conditions.

5.1. Scenario I, radiation only

Fig. 7 shows the particle surface temperature distribution (in the frontal view) for scenario I across all packing densities under radiative heating from the top wall set at 2573.15 K. The colour scale represents temperature, with red indicating higher temperatures and blue indicating lower temperatures. Particles enter the domain (left) at a low temperature and progressively heat up as they move towards the opposite side (right). The residence time of the particles in the domain is 54 s in the 540-sphere case, and 256 and 500 s in the other two cases, respectively (see Table 2).

In all three cases, the particle temperature distribution is rather “skewed”. Distinct temperature gradients are visible in vertical and horizontal directions. This is an immediate effect of the different a) bulk porosities and b) bulk velocities.

The heating of the particles originates from radiation by the high-temperature top wall, which first heats up particles that are visible to the wall. These are mostly particles in the bulk's upper layer, but radiation can already penetrate deeper into lower layers, depending on the local packing porosity. As the temperature of the upper layer particles increases, the particles emit more radiation and contribute to the heating of the particles with lower temperatures, which are in layers below. Thus, a radiative heating front penetrates through the bulk in vertical direction.

Due to the bulk motion, particles in the upper layer are not heated up homogeneously. Instead, as the particles are moving from left to right, particles that are further at the outlet have received more heat and are at higher temperatures. This also means that the radiative heating front in the vertical direction already penetrated deeper layers of the bulk at this position.

As the velocities (residence times) are different for the three cases, the particles in the upper layer(s) also depict different heating behaviour, which in turn affects the progression of the heating front in vertical direction. This phenomenon will be discussed based on incident radiation G further below.

Fig. 8 shows temperature histograms, i.e., the percentage of particles (relative to the total number of particles in each case) versus their surface temperatures for scenario I. In Fig. 8(a), the

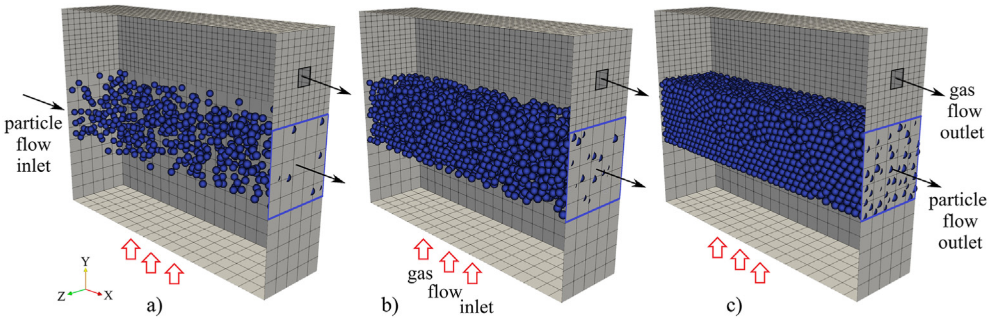

Fig. 5. Three distinct moving bulk cases: (a) dilute case composed of 540 spheres (b) moderate case composed of 2560 spheres (c) dense case composed of 5000 spheres.

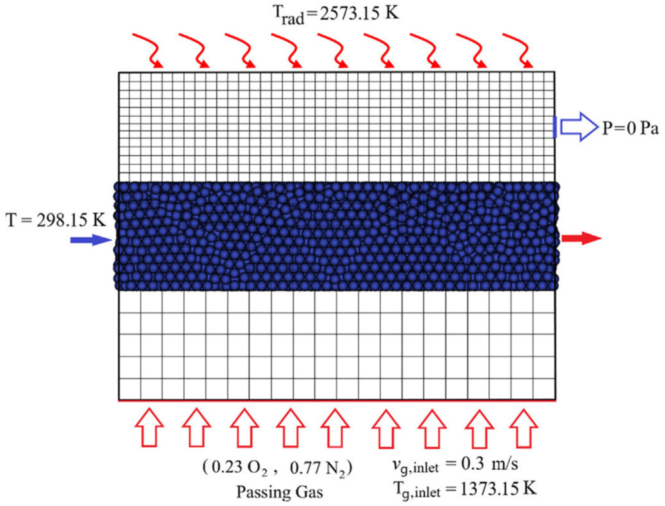

Fig. 6. Boundary conditions.

Table 2
Bed porosity (∅), velocity of particles ($v_{spheres}$), particle mass flux ($\dot{m}_{spheres}$), and the time required for one particle to move from the left to the right of the box ($t_{residence}$) for the three cases. *N* shows the number of particles, and $v_{g,inlet}$ represents the gas velocity at the entrance of the domain.

Parameter	Unit	Dilute	Moderate	Dense
N	[−]	540	2560	5000
∅	[%]	93	66.5	34.5
$v_{spheres}$	[m/s]	0.00743	0.00156	0.0008
$\dot{m}_{spheres}$	[kg/s]	0.003665	0.003665	0.003665
$t_{residence}$	[s]	54	256	500
$v_{g,inlet}$	[m/s]	0.3	0.3	0.3

particles for the 540-, 2560-, and 5000-sphere case have different residence times as listed in Table 2. In Fig. 8(b), the residence times for 540-, 2560-, and 5000-sphere are identical with the residence time of the 540-sphere case listed in Table 2. The reason for the selection of an additional simulation setup with same residence time will be explained later.

The left side of each graph in Fig. 8 represents the particles at low temperatures near the particle inlet, as well as those in the bottom layer. The right side of the graphs represent the particles at high temperatures, which are those closest to the particle outlet, specifically, the top layer.

For the 5000-sphere case in Fig. 8(a), some particles in the upper layers reach temperatures as high as 1567 K due to their long exposure to radiation (the longest residence time in the domain). In contrast, the maximum temperatures reached in the 2560- and 540-sphere case are 1347 and 1400 K, respectively. The temperature of the 540-sphere case is slightly higher than for the 2560-sphere case, although the residence time is significantly lower for the 540-sphere case. This can be explained with the higher visibility (higher bulk porosity) of the spheres in the 540-sphere case: Not only does the radiation penetrate better in vertical direction, also transfer in horizontal direction is increased for the 540-sphere case. This means that particles in the upper layer, once heated, contribute to the heating of neighbouring particles in the same layer. Even though the residence time is shorter in the 540-sphere case, the cross-heating due to better visibility compensates for it.

There is a peak on the left side of the histogram for both the 2560-sphere and 5000-sphere cases, which corresponds primarily to particles at lower temperatures in the bottom layer as well as the incoming particles. This peak is absent in the 540-sphere case since nearly all bottom particles receive radiation directly from the top wall and only a few particles close to the particle inlet are at low temperature.

To isolate the effect of bulk porosity on the radiation field and temperature distribution, another test was performed where particles in all three cases move at the same velocity as in the 540-sphere case, i.e., they have the same residence time of 54 s in the domain. The results are shown in Fig. 8(b). As the residence time for the 2560-sphere and 5000-sphere is now much smaller than before, the number of particles at low temperatures increases significantly in both cases. As a result, the left peak in the diagram increases from approximately 3% to over 12%. The maximum temperature decreases from 1347 K to 1179 K in the 2560-sphere case and from 1567 K to 1320 K in the 5000-sphere case due to reduction in the residence time. Again the 540-sphere case shows the highest temperatures with values up to 1400 K due to the “visibility effect” explained above.

Fig. 9 shows the incident radiation *G* within the domain in [W/m^2] as described in Eq. (11). Fig. 9(a) shows the results for different particles residence times and Fig. 9(b) for the same residence time. The local *G* values reflect the penetration depth of radiation through the particle bed. The region containing the particles is highlighted in green with rows of fluid cells in this area numbered

Table 3
Simulation parameters.

Parameter	Symbol	Unit	Value
CFD time step	Δt	[s]	0.0002
Domain size	$\Delta x \times \Delta y \times \Delta z$	[m^3]	0.4 × 0.2 × 0.02
Mesh size in the bulk region	$\Delta x \times \Delta y \times \Delta z$	[m^3]	0.02 × 0.02 × 0.02
Particle radius	R	[m]	0.005
Particle density	ρ_p	[kg/m^3]	700
Particle emissivity	ε_p	[−]	0.85
Particle absorption coefficient	a_p	[m^{-1}]	Eq. (17)
Particle thermal conductivity	k_p	[W/m·K]	0.19
Particle Poisson's ratio	ν_p	[−]	0.35
Particles specific heat capacity	$c_{p,p}$	[J/(kg·K)]	1500
Particles Young's modulus	Y	[Pa]	$10e^{+9}$
Gas thermal conductivity	k	[W/m·K]	0.04
Gas absorption coefficient	a_g	[m^{-1}]	0
Gas emissivity	ε	[−]	0
Absorption coefficient of top wall	a_w	[m^{-1}]	0.7
Absorption coefficient of all walls except top wall	a_w	[m^{-1}]	1
Emissivity of top wall	ε_w	[−]	0.7
Emissivity of all walls except top wall	ε_w	[−]	1

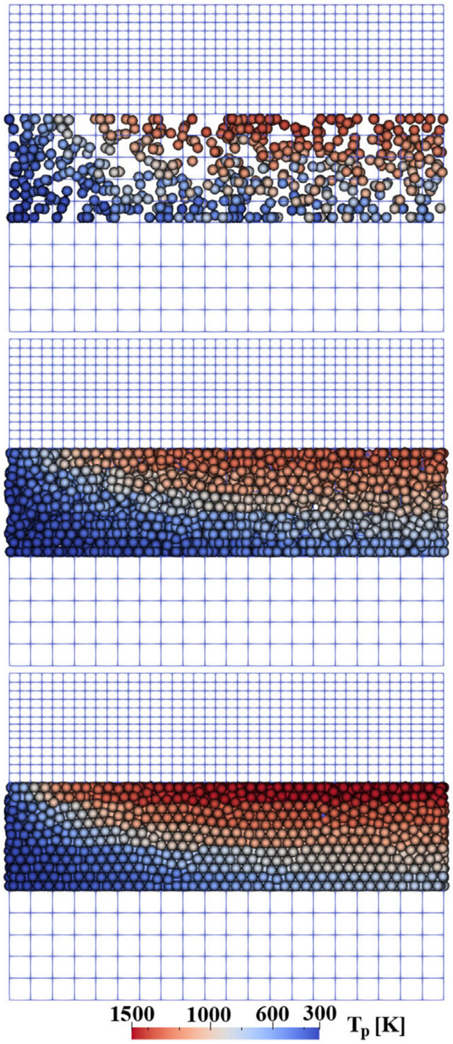

Fig. 7. Frontal view: particle surface temperature distribution due to radiative heat transfer in 540 (top), 2560 (middle), and 5000 (bottom) sphere cases (scenario I).

from 1 to 5. This numbering will help clarify the discussion in the following section.

Fig. 9(a) indicates that for all three packing densities, radiation reaches the lowest layer of particles. The radiation penetration depth in the 5000-sphere case is larger than in the other cases, which is related to the larger residence time of the particles in the domain compared to the 2560- and 540-sphere cases. The densely packed upper sphere layer in the 5000-sphere case receives more radiation from the top wall and with sufficient time, the particles of the top layer will emit more radiation to the lower layers, leading to a larger penetration depth of radiation. The 540-sphere case exhibits larger penetration in horizontal direction compared to the 2560-sphere case, as seen on the left side of rows 2 and 3 in Fig. 9(a) (more red-coloured fluid cells with high G). These higher values can be attributed to the lower packing density, which allows for higher visibility of the spheres in horizontal direction. The already heated particles on the right side of layers 2 and 3, transfer more effectively heat towards the yet low-temperature neighbouring particles. This is because the lower packing density results in a smaller absorption coefficient in the DOM equations in horizontal direction. In the 540-sphere case, radiation also penetrates more effectively in the vertical direction, reaching strongly down to the 3rd layer in a shorter time (54 s) compared to the 2560-sphere case (256 s). The G values averaged for all fluid cells in the 2nd and 3rd rows are notably higher in the 540-sphere case, with 389.8 and 194.7 kW/m^2, compared to 313.5 and 148.7 kW/m^2 in the 2560-sphere case, respectively. Again, the more dispersed arrangement of particles (larger void space between particles) allows radiation to penetrate directly to the bottom layers compared to the other cases. This ultimately means that the lower packing densities compensate for the shorter residence times regarding heating, due to an improved visibility. This, however, is only true to some degree, as the residence time for the 5000-sphere case is so long, that the radiation can penetrate deeply into the bed due to the radiation of particles from the top layers, which are at high temperature, to the bottom layers. In fact, the 5000-sphere case exhibits the largest penetration depth, with an average G value, for instance, in the 2nd and 3rd rows are 566.9 and 291.8 kW/m^2, which exceeds the corresponding values in the two other packing densities. Summarizing, it can be said that residence time and packing porosity have a competing impact onto the penetration depth of radiation.

As can be seen in Fig. 9(b), under the condition of identical residence time, as expected, the 540-sphere case has the highest penetration depth compared to the other cases (deep red particles in the 3rd row of the CV cells) due to dispersed arrangement of particles (the large void fraction). In this case, the larger void fraction enables radiation to reach the lower layers of particles directly, and, therefore, the 540-sphere case shows the highest G values for all cases considered here. For other two cases, which have lower void fractions, the radiation front is penetrating only about halfway through the bulk - significantly less than in the 540-sphere case. However, for the denser cases, radiation absorption in the dense top layers and its subsequent transfer to the lower layers becomes more important. This effect is stronger for the denser packed beds. This is why the values of G in the 5000-sphere case are larger than those in the 2560-sphere case in the upper layers. For example, in the second row, average G value is 132.42 kW/m^2 in the 2560-sphere case and 171.08 kW/m^2 in the 5000-sphere case.

The average G values in row 5 are 36.4, 1.96, and 0.84 kW/m^2 in 540-, 2560- and 5000-sphere case, respectively. This means that only in the 540-sphere case, the lowest particle layers really receive direct radiative heat from the top wall. For the two other cases with lower bed porosity, the G values are almost negligible with slightly larger values for the 2560-spheres case due to its lower packing density.

Fig. 10 shows the average particle surface temperatures at the outlet of the domain. In Fig. 10(a) (different residence times), the average particle temperatures at the outlet of the domain, $\overline{T}_{p,outlet}$, are 1024.1, 982.4, and 1160 K for the 540-, 2560-, and 5000-sphere cases, respectively. This indicates that the temperatures are ordered according to their incident radiation G (Fig. 9(a)) and not their bed porosity $\varnothing$. The 5000-sphere case shows the highest G in Fig. 9(a) ($\overline{T}_{p,outlet}$ 1160 K, $\varnothing = 34.5\%$) followed by the 540-sphere case ($\overline{T}_{p,outlet}$ 1024.1 K, $\varnothing = 93\%$), and then the 2560-sphere case ($\overline{T}_{p,outlet}$ 982.4 K, $\varnothing = 66.5\%$). The reason for this ordering has already been explained above.

In the cases with identical residence time (Fig. 10(b)), $\overline{T}_{p,outlet}$ values are 1024.1, 626.6, and 602 K for the 540-, 2560-, and 5000-sphere case, respectively. Here, the ordering is strictly based on bed porosity. For the 540-sphere case, higher G values, as previously discussed, are present in the region of the lower particle layers (Fig. 9(b)), leading to the highest $\overline{T}_{p,outlet}$.

For the 2560- and 5000-sphere cases, the average G values in the 4th and 5th rows are very small (2560: 9 kW/m^2 - 4th row, 1.94 kW/m^2 - 5th row; 5000: 7.3 kW/m^2 - 4th row, 0.84 kW/m^2 - 5th row), i.e. particle heating by radiation is almost negligible for

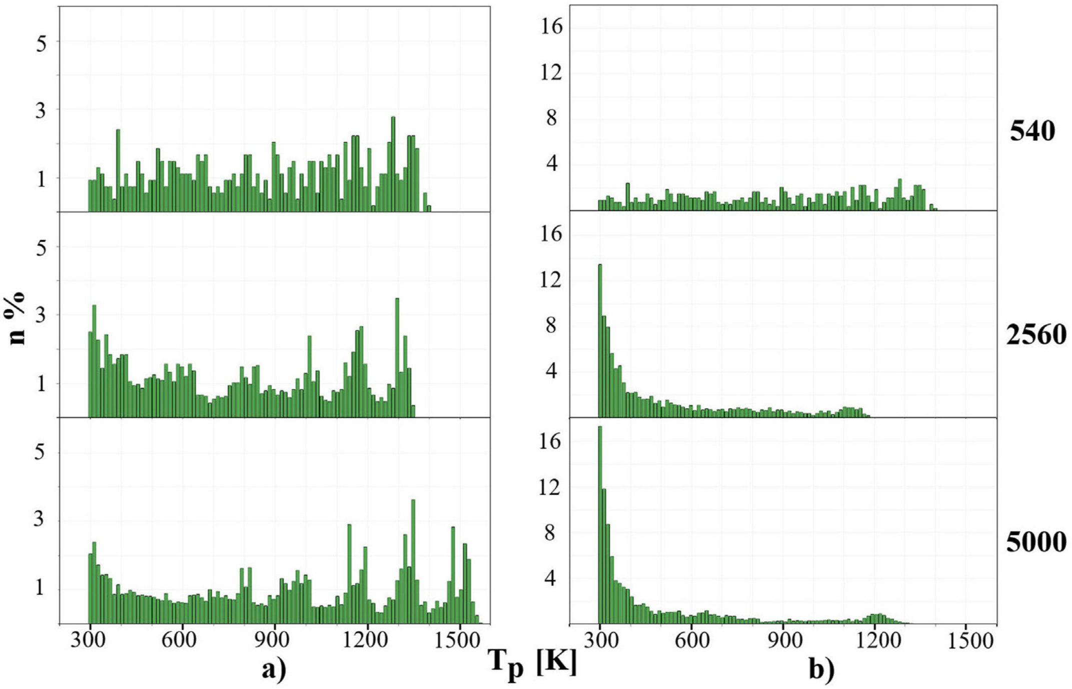

Fig. 8. Percentage of particles (relative to the total number of particles in each case) versus their surface temperature across the entire domain in 540 (top), 2560 (middle), and 5000 (bottom) sphere cases (scenario I). (a) Particle residence time based on Table 2. (b) Same particle residence as 540-sphere case.

both cases. Here, the larger number of particles at low temperatures in rows 4 and 5 for the 5000-sphere case become important, leading to a lower mean particle outlet temperature $\overline{T}_{p,outlet}$ compared to the 2560-sphere case). This occurs, although for the 5000-sphere case, the *G* values are larger in the upper rows (see section above). Thus, the many particles at low temperatures for the 5000-sphere case overcompensate the larger incident radiation in the upper layers.

For the cases with different residence times, the standard deviation of particle temperatures is 59.8, 23.8, and 8.3 K for the 540, 2560, and 5000-sphere (Fig. 10(a)), and for the cases with same residence time 59.8, 22.6, and 11 K (Fig. 10(b)), respectively. Thus, the standard deviation consistently decreases as the number of spheres increases, regardless of whether the residence times vary (Fig. 10(a)) or are the same (Fig. 10(b)). The 5000-sphere case has the smallest standard deviation in both Fig. 10(a) and (b). It shows that as the number of particles increases, the thermal energy tends to be more evenly distributed across the spheres, resulting in a lower standard deviation of temperature. In the 540-sphere case, individual particles may experience more significant fluctuations, leading to a larger spread of temperatures. Fewer particles mean that these variations are not averaged out as effectively as in denser systems.

5.2. Comparison of scenario II (convection), III (convection and conduction), IV (convection, conduction and radiation)

Fig. 11 shows the particle surface temperatures in the packed bed and the distribution of fluid temperature for the three scenarios II, III, IV. Arrows within the fluid domain represent the direction of airflow. Note that fluid inlet is not positioned directly at the lower layer of the particle bed, it is located 0.1 m below the bottom layer of spheres, i.e., gas velocity field upstream of the bed is influenced by the local bed porosity. This is particularly visible in the 540-sphere case for scenarios II and III (Fig. 11(a) and (b)). Here, a recirculation zone exists upstream of the bed at the right side of the domain, also indicated by the blue colour of the gas temperature. In this area, low-temperature gas from downstream of the bed flows back through the granular assembly. This is possible as bed porosity is low and the low flow resistance in the bed allows for backflow. Interestingly, the recirculation zone vanishes for scenario IV. Additional particle heating through radiation raises particle temperatures, which in turn increases gas temperatures, affecting the pressure and velocity field in a way that suppresses backflow. In the two cases with higher packing density, recirculation does not occur at all, as flow resistance in the bed is larger due to the lower bed porosity, and hence backflow is avoided.

In Fig. 11(a), scenario II, with just convective heat transfer, the particle surface temperatures in the 540-sphere case remain low. This is caused by the short residence time of the particles in the domain, along with the relatively small heat transfer coefficients in the bed (gas velocity is small due to the low packing density). The gas temperature downstream of the bed is locally enhanced as the gas is not able to transfer all its enthalpy to the particles.

For the 2560-sphere and 5000-sphere cases in Fig. 11(a), the situation is different. The longer particle residence together with the increased mean gas velocity in the bed (due to porosity reduction of the bed) leads to stronger heat up of the particles. This is mainly visible for the lower particle layers at the exit of the domain. The upper particle layers stay at relatively low temperatures, as the enthalpy of the gas is almost completely transferred to the lower particle layers. This also results in a low gas temperature downstream of the bed.

Fig. 11(b) shows the results for scenario III, where conduction between particles is incorporated along with convective heat transfer. The addition of conduction leads to noticeable changes in the temperature distribution for the 2560- and 5000-sphere configurations, while its effect is less significant in the 540-sphere case. This small effect in the 540-sphere case is due to the limited number of particles in contact. Convection dominates the heat

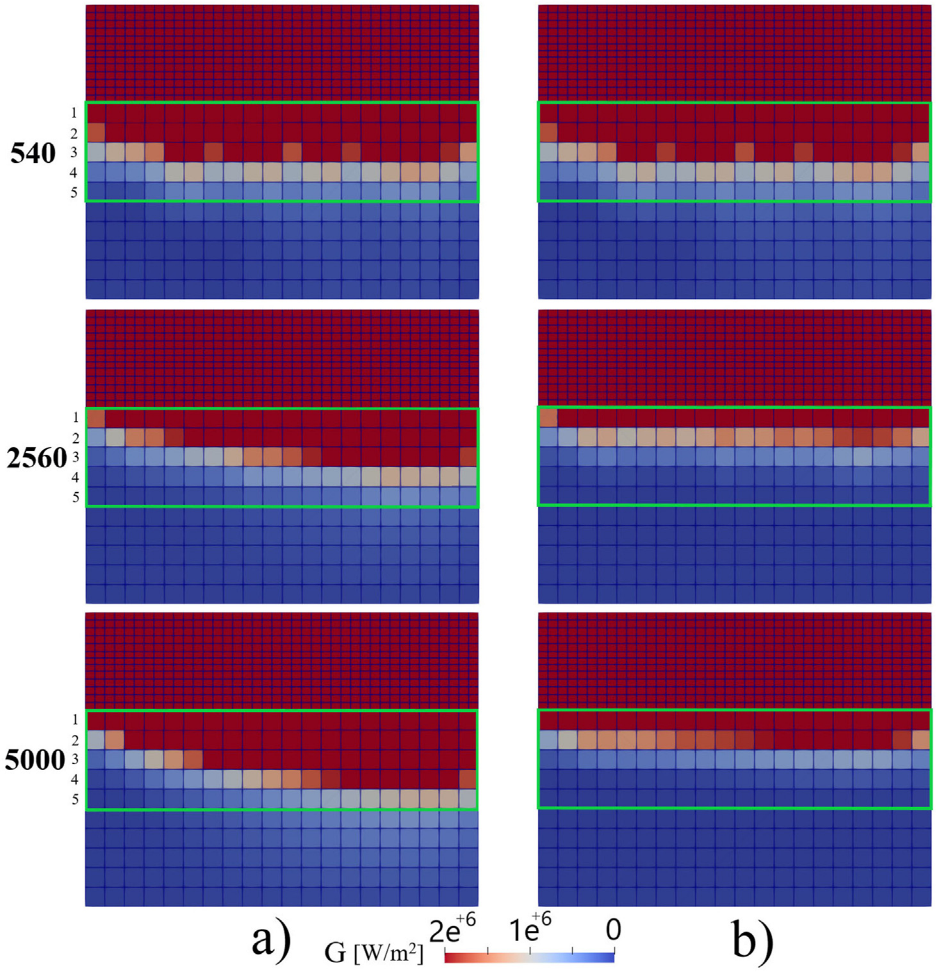

Fig. 9. Incident radiation contour in 540 (top), 2560 (middle), and 5000 (bottom) sphere cases (scenario I). (a) Different residence time based on Table 2. (b) Same residence time as 540-sphere case.

transfer mechanism here. The number of contacts is 207, 4318, 16589 in the 540-, 2560-, and 5000-sphere cases, respectively.

The most notable changes occur in the 5000-sphere configuration. Conduction effectively transfers heat between particles of different temperature in this densely packed bed, causing the top layers to heat more rapidly than before. The temperature gradients are less steep compared to the convection-only scenario II in Fig. 11(a).

Fig. 11(c), the combination of convection, conduction, and radiation (scenario IV), provides the most uniform heating across all configurations. The introduction of radiation from the top wall enhances the heating of particles, especially in the upper layers.

The upper particles in the 540-sphere case, which previously remained at low temperatures due to the limited impact of convection, show now elevated temperatures due to radiative heat transfer from the top. The top layer of particles at the outlet reaches a maximum temperature of 1291 K, while some particles in the bottom layer at the outlet have a temperature of 1055 K.

Radiation has a strong effect in the denser configurations. The high-temperature zones expand as radiation heats the top layers, which were at lower temperatures due to limited convection and conduction. The previously observed temperature gradient between the top and bottom layers is substantially reduced. In the 2560 and 5000-sphere cases, the upper layers now reach temperatures slightly larger than those of the lower layers.

In all the three different packing density cases, the gas temperature downstream of the bed is now high, in contrast to scenario II and III. This occurs because the particles with high temperatures in the top layers transfer significant heat by convection to the gas phase and not all the heat supplied to the system can be stored in the particles.

Fig. 12 displays histograms of particle surface temperature distributions for each heat transfer mode (scenarios II, III, and IV) and for each packing density (540, 2560, and 5000 spheres). The particles with high temperatures on the right side of each graph are those closest to the particle outlet—specifically, the bottom layer in scenarios II and III and the top layer in scenario IV. Conversely, the left side of the graphs represents particles with low temperature near the particle inlet, as well as those in the top layer in scenarios II and III.

For scenario II (just convection Fig. 12(a)), the 540-sphere case exhibits a narrow histogram of almost symmetric shape with the particles reaching a maximum temperature of 856 K. The temperatures at the right side of the graph remain relatively low due to the short residence time of the particles in the domain (54 s). A few particles are at their initial low temperature (298 K), corresponding to the incoming particles. In the denser cases, the particle temperature distributions are broader, reaching maximum temperatures up to 1322 K (2560-sphere case) and 1348 K (5000-sphere case), i.e., some particles reach almost gas temperature

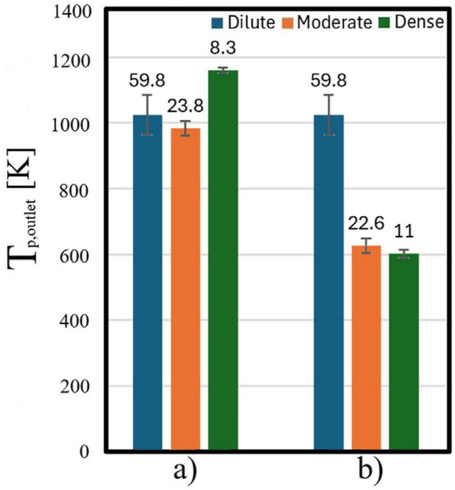

Fig. 10. Average particle surface temperatures at outlet of the domain $\overline{T}_{p,outlet}$ and the standard deviation (as numbers) in 540 (blue), 2560 (orange), and 5000 (green) sphere cases (scenario I). (a) Different residence times based on Table 2. (b) Same residence time as 540-sphere case.

(1373.15 K). This can be attributed to the extended particle residence times of 256 s (2560-sphere case) and 500 s (5000-sphere case). A peculiarity of the histogram of the 5000-sphere case is its rather asymmetric shape with a peak at low temperatures; many particles stay near their initial temperature (298 K). Particularly, in the entrance area of the domain, the many low-temperature particles in the bottom layers consume most of the heat delivered by the gas with the consequence that the upper layers receive no convective heat and stay at low temperatures. A second peak is located at higher temperature around 1200–1300 K, which is caused by the particles in the bottom layers at the domain outlet. These particles reach almost gas temperature. In the 2560-sphere case, a broad distribution can be observed too. The shape of the histogram falls between the symmetric shape seen in the 540-sphere case and the asymmetric shape in the 5000-sphere case. In the 2560-sphere case, nearly all particles are heated up, and the left peak does not occur in this case. Only a few particles reach the fluid inlet temperature, as they remain in the domain for approximately half the duration compared to the 5000-sphere case.

The histogram for the 540-sphere case in Fig. 12(b) (scenario III, convection and conduction) shows that the temperature distribution remains similar to the convection-only case (scenario II). This is caused by the small number of direct particle contacts for this low packing density configuration, i.e., the contribution of contact heat transfer is small. In the denser cases, the introduction of conduction results in an equilibration of the temperatures in the packing compared to the convection-only scenario II. Fewer particles remain at their initial low temperature, but more particles reach higher temperatures, particularly in the 5000-sphere case.

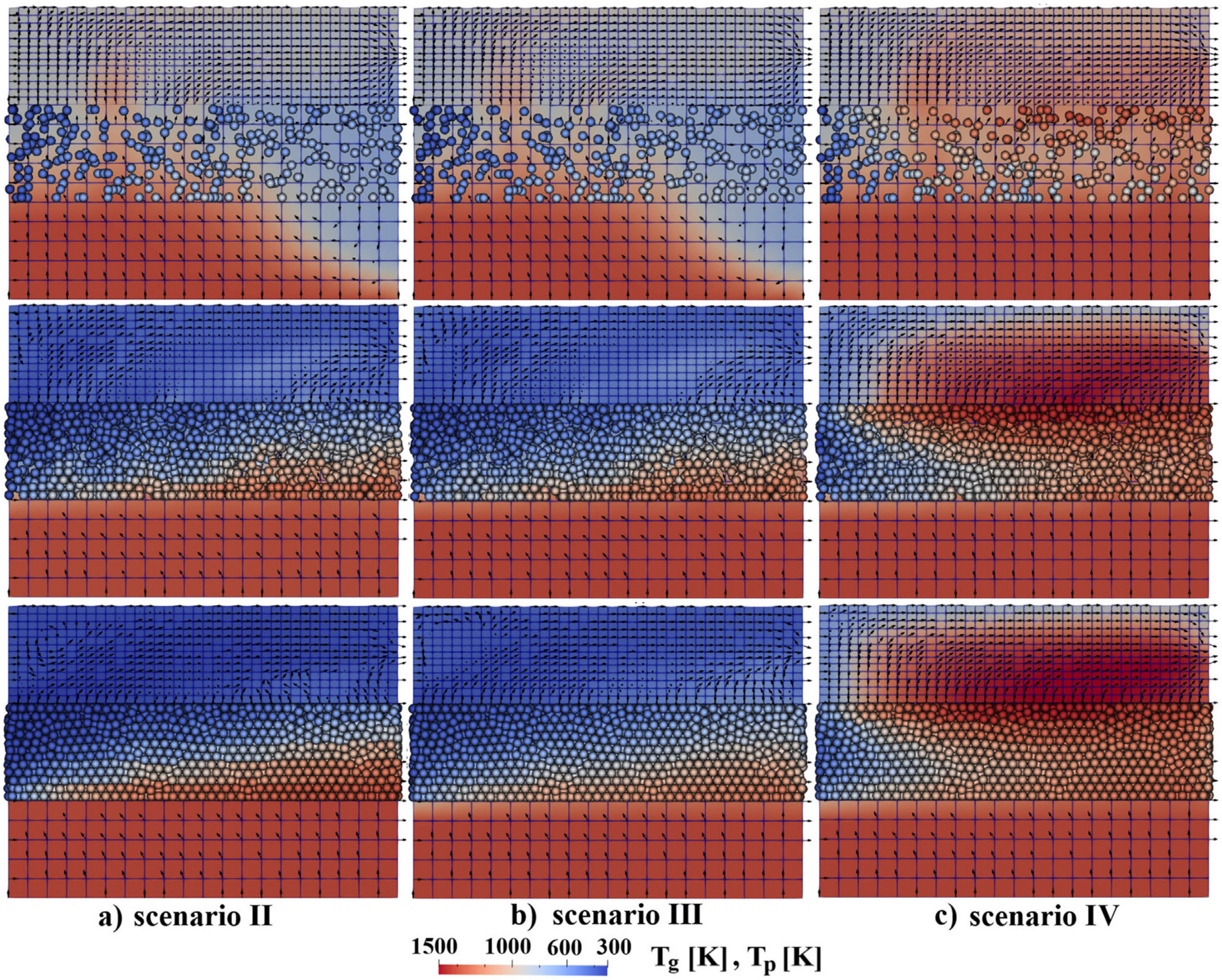

a) scenario II

b) scenario III

c) scenario IV

Fig. 11. Frontal view: particle surface temperature distribution across various heat transfer modes: (a) convective heat transfer (scenario II), (b) convective heat transfer plus conduction among particles (scenario III), (c) convective heat transfer and conduction among particles plus radiation (scenario IV).

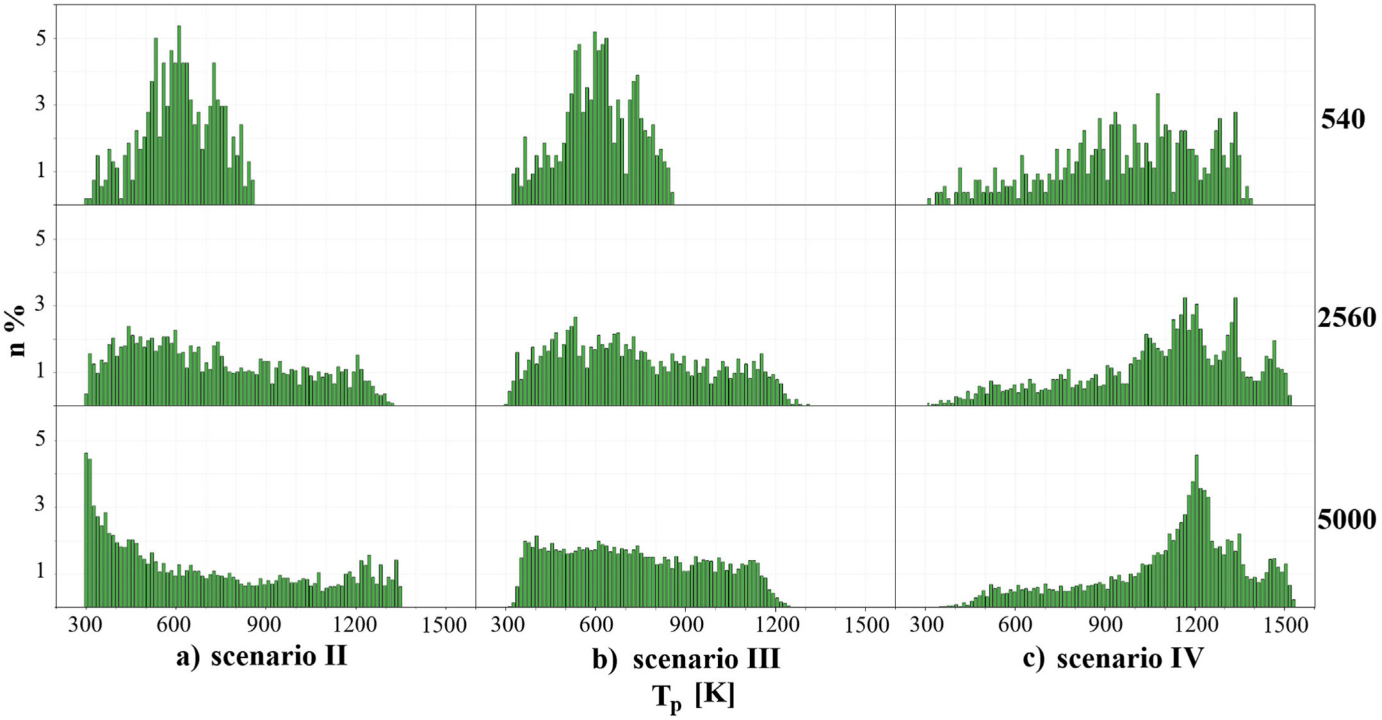

Fig. 12. Percentage of particles (relative to the total number of particles in each case) versus their surface temperature across the entire domain in 540 (top), 2560 (middle), and 5000 (bottom) sphere cases. (a) Convective heat transfer (scenario II), (b) convective heat transfer plus conduction among particles (scenario III), (c) convective heat transfer and conduction among particles plus radiation (scenario IV).

Although more particles reach higher temperatures, the number of particles reaching the highest temperature decreases. The maximum temperatures decrease from 1322 K to 1309 K (2560-sphere case) and from 1348 K to 1244 K (5000-sphere case). This reflects the enhanced heat transfer due to conduction, which helps to distribute heat more evenly across the particle bed.

As can be seen in Fig. 12(c), radiation has a significant effect on the temperature distribution (scenario IV: convection, conduction and radiation). The histograms become right-skewed due to the strong effect of radiation. For the 540-sphere case, the histogram shows that more particles reach higher temperatures compared to scenario II and III, indicating that radiative heat transfer from the top wall accelerates the heating of the particles drastically, particularly those in the upper layers. Radiation dramatically shifts the temperature distributions in the denser configurations. Most particles in all packing densities now reach temperatures above 1000 K. This shift indicates that radiation is the dominant heat transfer mechanism, overcoming the limitations of convection and conduction. The particles reach a maximum temperature of 1386 K in the 540-sphere case, 1516 K in 2560-sphere case and 1529 K in 5000-sphere case.

A comparison of the temperature histograms of scenario IV, which includes convection, conduction, and radiation (Fig. 12(c)), and the radiation-only scenario I (Fig. 8(a)) offers insight into the contribution of the different heat transfer mechanism. Of course, across all three packing densities, the inclusion of conduction and convection in Fig. 12(c) results in higher overall particle temperatures than in the radiation-only scenario I in Fig. 8(a). As a result, the left peak in the temperature distribution, which corresponds to particles at lower temperatures, is noticeably reduced in Fig. 12(c) for all packing densities.

In the 540-sphere case, the temperature distribution changes slightly when comparing the radiation-only scenario I to the full heat transfer scenario IV. In the full heat transfer scenario, fewer particles are at the low temperature end of the histogram. Particularly, this shift is related to the fact that bottom layer particles now receive heat due to convection.

In the 2560-sphere cases, the maximum temperature increases from 1347 K in the radiation-only scenario I to 1516 K in the full heat transfer scenario IV. In scenario IV, the particles in the bottom layers receive convective heat by the gas, and the particle temperature increases in the bottom layer. Consequently, they can absorb significantly less heat from the high-temperature particles in the top layer, allowing the top layer particles to further increase in temperature through radiation. This leads to the increase in maximum particle temperatures.

In contrast, in the 5000-sphere cases, the maximum temperature decreases from 1567 K in the radiation-only scenario I to 1529 K in the full heat transfer scenario IV. Due to increased conduction from the higher packing density, the maximum temperature is slightly reduced, resulting in a smoother temperature distribution throughout the domain, as shown in Fig. 11(c) (scenario IV).

Fig. 13 presents the average particle temperatures at the outlet of the domain, $\overline{T}_{p,outlet}$, for scenario II, III, and IV.

In scenario II (Fig. 13(a), convection only), the outlet temperature is ordered based on particle residence time. As a result, the 5000-sphere case has the largest outlet temperature, followed by the 2560-sphere case, and then the 540-sphere case. When conduction is introduced (scenario III, Fig. 13(b)), the outlet temperature for the 540-sphere case remains the same, but interestingly, the outlet temperatures for the 2560-sphere and 5000-sphere cases, decrease slightly. The explanation for this behaviour is that conduction equilibrates the temperatures in the bed and leads to reduction of the driving temperature difference between gas and particles for convective heat transfer. This is, for example, documented by the decrease of the convective heat transferred to the

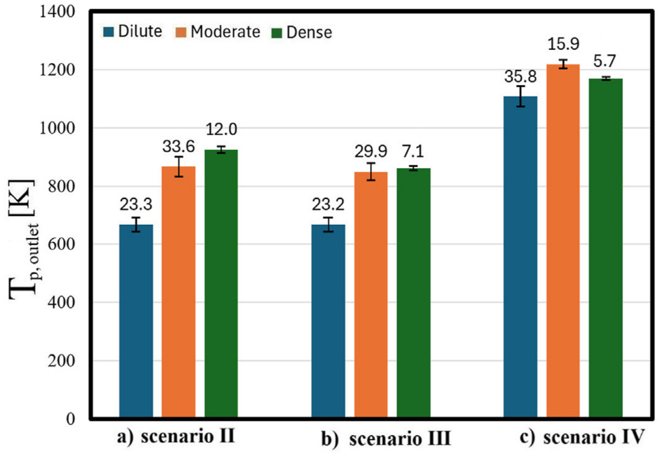

Fig. 13. Average particle temperatures at the outlet of the domain $\overline{T}_{p,outlet}$ and the standard deviation (as numbers) in 540 (blue), 2560 (orange), and 5000 (green) sphere cases. (a) Convective heat transfer (scenario II), (b) convective heat transfer plus conduction among particles (scenario III), (c) convective heat transfer and conduction among particles plus radiation (scenario IV).

particles for the 2560-sphere case. Here, the convective heat transfer to the particles is reduced from 3117 W (scenario II, convection only) to 3057 W (scenario III, convection and conduction). As the 5000-sphere case is the most densely packed, the impact of conduction is also the largest. This clearly shows the importance of conduction in very densely packed beds. When adding radiation (Fig. 13(c)), an increase in $\overline{T}_{p,outlet}$ occurs across all packing densities.

The smaller standard deviation in Fig. 13(b) (scenario III) compared to Fig. 13(a) (scenario II) across intermediate and dense packing densities indicates better temperature uniformity. This confirms that conduction effectively reduces temperature disparities among particles. As can be seen in Fig. 13(c) (scenario IV), adding radiation promotes more uniform heating in the 2560- and 5000-sphere cases documented by lower standard deviation compared to scenario II and III. This is because in scenario IV the particles in the top layers are now intensively heated by radiation. While the top layer particles stay at relatively low temperature without radiation, they now depict higher temperatures and, thereby, contribute to a lower standard deviation. In contrast, for the 540-sphere case, standard deviation increases for scenario IV. While the high-temperature fluid flow (scenarios II/III) already managed to heat up the particles in all layers quite equally, particles in the top layers are now at much higher temperature than in the lower layers due to radiation, thereby increasing the spread of temperature in the bed and, hence, standard deviation.

Of course, the outlet particle temperature is larger for scenario IV (Fig. 13(c)) compared to scenario I (Fig. 10(a)) for all packing densities, as additional heat is supplied form outside to the system by convection. However, the standard deviation is lower for scenario IV compared to scenario I, indicating that radiation alone does not promote uniform heat distribution as effectively as the combination with convection and, particularly, conduction.

5.3. *Individual contribution of the heat transfer mechanisms to bed heating, scenario IV*

To elaborate which heat transfer mechanism dominates, scenario IV is analysed further concerning the heat fluxes delivered to the particles from outside (convection and radiation). The data clearly shows that radiation is the dominant heat transfer mechanism, as the instantaneous radiative heat transferred to the particles in the 540-, 2560-, and 5000-sphere measures 3302, 4577, and 4495 W, respectively. In contrast, the heat transferred via convection is only 1069, 548, and 380 W, respectively.

The result for convection is surprising at first glance, as convective heat of the 540-sphere case is significantly larger (1069 W) than for the 5000-sphere case (380 W). For two reasons, one would expect the opposite: First, porosity in the 5000-sphere case is lower, and, hence, the mean gas velocity, and, consequently, the heat transfer coefficient is larger than in the dilute packing. Second, the number of particles in the dense packing is around 10 times larger than for the dilute packing.

This opposing trend can be explained as follows: a) particles can gain or lose heat through convection depending on whether the temperature difference between gas phase and particle is positive or negative. For the 5000-sphere case, the particles receive a +2110 W from the gas phase whereas the particles transfer −1730 W to the gas phase, leading to the net value of 380 W. In comparison, for the 540-sphere case the particles receive +1213 W from the gas phase whereas the particles transfer −144 W to the gas phase, leading to the net value of 1069 W. This means that, for the 540-sphere case, in most areas of the particle bed the gas temperature is above the particle temperature, except for the particles in the top layer towards the exit of the domain, where some high-temperature particles transfer heat to the gas phase. In contrast, in the 5000-sphere case there are distinctive larger areas where the driving temperature is positive or negative. Particles receive convective heat in the entrance area of the domain and in the bottom layers, where particles are at a low temperature, but also lose significant convective heat as many

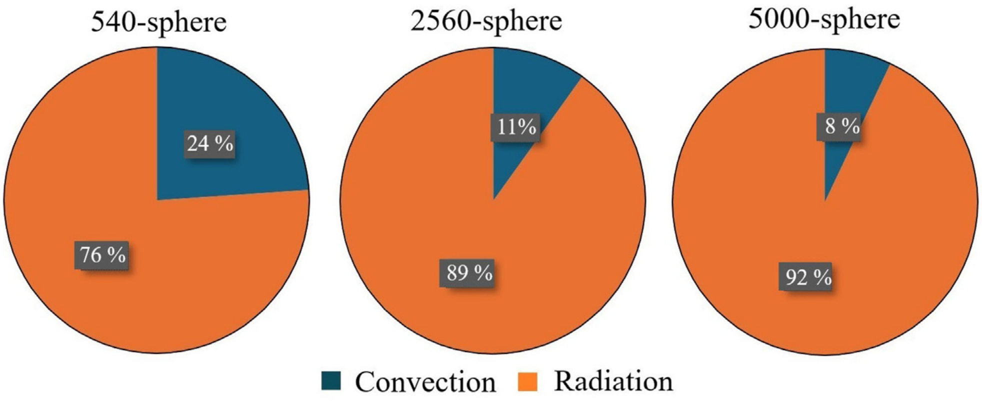

Fig. 14. Contribution of convection and radiation to the heat stored in the particles in heat transfer scenario IV for the different packing densities (540, 2560, and 5000 spheres).

particles above gas temperature exist in the top layers (highest radiation penetration depth as discussed before). b) when calculating the mean temperature difference between the gas phase and the particle, which drives the convective heat transfer to the particles, this difference is 230 K for the 540-sphere case, but only 20 K for the 5000-sphere case. This lower driving temperature difference compensates for the high particle number in the calculation of the convective heat flux.

The net effect is illustrated in the pie charts in Fig. 14. It presents the relative contributions of convection (blue) and radiation (orange) to the heat stored in the solid phase for the three different packing densities. In all configurations, radiation is the dominant heat transfer mechanism, accounting for 76% in the 540-sphere case, 89% in the 2560-sphere case, and 92% in the 5000-sphere case. This demonstrates that radiation becomes increasingly significant as packing density increases.

6. Summary and conclusion

This study employed the Discrete Ordinates Method (DOM) within the framework of a coupled Discrete Element Method and Computational Fluid Dynamics (DEM-CFD) model to effectively simulate radiative heat transfer in granular particle systems. The Averaged Volume Method is used, in which time-varying source terms and a porosity field, integrated into the Navier-Stokes equations, represents the inclusion of particles. Incorporating local bed porosity into the equations of particle emission, particle absorption, and radiation propagation allows to consideration of different packing densities. The absorption and emission coefficients have been adapted such that a consistent balance occurs across different packing densities. The accuracy of the DOM model is validated by comparing its results with both the P1 radiation model and experimental data for a bed of spherical particles.

A numerical test case has been set up to investigate the interaction between heated walls, moving particle layers with prescribed velocity, and passing air in cross flow with the particles. The particles are heated by the top wall (2573.15 K) of the simulation domain and by the cross flow of air (1373.15 K) with a constant inlet velocity of 0.3 m/s. Conduction between particles is considered too. Four scenarios have been formulated and analysed: scenario I (just radiation), scenario II (just convection), scenario III (convection and conduction), scenario IV (convection, conduction and radiation). Three granular assemblies with different packing densities are considered: dilute (bed porosity 93%), moderate (bed porosity 66.5%), and dense (bed porosity 34.5%). The dilute, moderate, and dense cases consist of 540, 2560, and 5000 randomly distributed spheres, respectively. The spheres travel along a fixed path within a rectangular domain, gradually increasing in temperature as they progress toward the exit. The incoming particle mass flow has been set constant, i.e., the three cases show different particle residence time in the simulation domain. The 540-sphere case shows the lowest residence time (54 s), whereas 5000-sphere case has the largest residence time (500 s). In addition, for scenario I (just radiation), an additional simulation setup is considered, where particles in the 2560- and the 5000-sphere case have the same residence time as in the 540-sphere case.

A thorough discussion explains the temperature distribution within both the fluid domain and the particle domain for the different scenarios and packing densities. For scenario I, the incident radiation field G [W/m^2] for the different cases is additionally presented. The results show that:

- Given the selected boundary conditions, with the top wall being at a temperature of 2573.15 K, radiation is the dominating heat transfer mechanism.
- When particles travel with the same residence time through the domain, the radiation penetration depth (with the incident radiation flux G being the quantitative measure) is a sole function of packing density. Low packing densities, i.e., high porosities, increase the visibility of the particles for the radiation emitted from the top wall. Therefore, the mean particle outlet temperatures follow this trend; the dilute packing has the highest mean particle temperature followed by the moderate and dense packing.
- When particle travel with different residence times, 54 s (dilute packing), 256 s (moderate packing), and 500 s (dense packing), the statement above concerning particle outlet temperatures holds true for the sequence of dilute and moderate packing. Different compared to the same residence results, the dense packing shows the highest radiation penetration depth. Due to the large residence time, the top layer of particles that faces the heated top wall receives a significant amount of radiation, thereby, increasing particle temperature. When the particle travel through the domain, they emit radiation to the lower particle layers, i.e., penetration depth is no longer dominated by wall-particle radiation, but by particle-particle radiation within the bed.
- In scenario IV, as packing density increases, the contribution of convective heat transfer decreases significantly, while radiation becomes the primary mechanism of heat transfer. In the 540-sphere case, convection accounted for 24% of the total heat transfer, but this proportion dropped to just 11% in the 2560-sphere case and 8% in the 5000-sphere case. The high importance of convective heat transfer for the 540-sphere case compared to the more densely packed cases is not intuitive, as the 540-sphere case has the lowest mean gas velocities in the bed (highest porosity) associated with a low heat transfer coefficient and the smallest number of particles. The analysis showed that for the 540-sphere case, the particles primarily gain heat from the gas phase and experience only minimal heat loss. In contrast, for the 5000-sphere case, the particle assembly gains substantial convective heat from the gas phase but also loses a significant amount back, resulting in a low net convective heat transfer to the particles. This could be traced back to the quite different spatial temperature distributions in the two configurations. The low net convective heat transfer to the particles in the 5000-sphere is also reflected in the small mean driving temperature difference for convection of just 20 K compared to 230 K for the 530-sphere case.
- The inclusion of particle-particle conduction promotes a more uniform temperature distribution across the particle bed and helps to reduce temperature disparities among particles. This effect is especially pronounced in the higher-density configurations where particle-particle contacts are most frequent.
- The study also demonstrates that in densely packed particle systems in scenarios II and III, the enthalpy of the inlet gas is almost entirely transferred to the lower particle layers, leaving the upper particles at relatively low temperature.
- Adding radiation promotes more uniform heating in the denser packing configurations compared to scenarios II and III. Radiation becomes more important in these denser cases, as it can penetrate through all particle layers, and effectively heating the entire bed in scenario IV. This leads to more uniform heating of the particles, as evidenced by the temperature profiles, histograms, and outlet temperature measurements.
- Overall, denser systems exhibit the smallest standard deviation of particle outlet temperature in all cases, reflecting the most uniform temperature distribution.

This work provides insights into the complex interactions between convection, conduction, and radiation of moving packed beds, particularly on the influence of packing density on heat transfer. It enhances the understanding of the thermal behaviour in such systems and offers a comprehensive framework for simulating heat transfer in industrial applications where granular materials are exposed to high temperatures.

CRediT authorship contribution statement

Rezvan Abdi: Writing – original draft, Visualization, Validation, Software, Investigation, Formal analysis. **Bo Jaeger:** Writing – review & editing, Software, Formal analysis. **Enric Illana:** Writing – review & editing, Software. **Siegmar Wirtz:** Writing – review & editing, Supervision. **Martin Schiemann:** Writing – review & editing. **Viktor Scherer:** Writing – review & editing, Supervision, Project administration, Methodology, Formal analysis, Conceptualization.

Declaration of competing interest

The authors declare that they have no known competing financial interests or personal relationships that could have appeared to influence the work reported in this paper.

Acknowledgement

This work has been funded by the Deutsche Forschungsgemeinschaft (DFG, German Research Foundation) – Project-ID 422037413 – TRR 287. Gefördert durch die Deutsche Forschungsgemeinschaft (DFG) – Projektnummer 422037413 – TRR 287.

References

Chandrasekhar, S. (1950). *Radiative transfer* (1st ed.). Oxford: Oxford University Press.

De Beer, M. (2014). *Characterisation of thermal radiation in the near-wall region of a packed pebble bed, Master's thesis*. North-West University.

Dombrovskii, L. A. (1997). Evaluation of the error of the P1 approximation in calculations of thermal radiation transfer in optically inhomogeneous media. *Teplofizika Vysokikh Temperatur, 35*(4), 684–688.

Dombrovsky, L. A. (2010). Estimate of P1 error for optically inhomogeneous media. https://thermopedia.com/content/134/. (Accessed 25 March 2021).

Ergun, S. (1952). Fluid flow through packed columns. *Chemical Engineering Progress, 48*(2), 89.

Forgber, T., & Radl, S. (2018). A novel approach to calculate radiative thermal exchange in coupled particle simulations. *Powder Technology, 323*, 24–44.

Gnielinski, V. (1980). Wärme-und stoffübertragung in festbetten. *Chemie Ingenieur Technik, 52*(3), 228–236.

Heaslet, M. A., & Warming, R. F. (1965). Radiative transport and wall temperature slip in an absorbing planar medium. *International Journal of Heat and Mass Transfer, 8*(7), 979–994.

Illana Mahiques, E., Brömmer, M., Wirtz, S., & Scherer, V. (2023). Locally resolved simulation of gas mixing and combustion inside static and moving particle assemblies. *Chemical Engineering & Technology, 46*(7), 1362–1372.

Jaeger, B., Illana Mahiques, E., Wirtz, S., & Scherer, V. (2023). Pyrolysis of spherical wood particles in a packed bed–comparison between resolved and unresolved discrete element method/computational fluid dynamics. *Chemical Engineering & Technology, 46*(10), 2120–2132.

Jaeger, B., Schlag, M., Scherer, V., Wirtz, S., & Schiemann, M. (2021). Radiative heat transfer with a blocked-off approach for application in the discrete element method. *Powder Technology, 392*, 558–569.

Krause, B., Liedmann, B., Wiese, J., Bucher, P., Wirtz, S., Piringer, H., & Scherer, V. (2017). 3D-DEM-CFD simulation of heat and mass transfer, gas combustion and calcination in an intermittent operating lime shaft kiln. *International Journal of Thermal Sciences, 117*, 121–135.

Mačak, J., Goniva, C., & Radl, S. (2023). Predictions of the P1 approximation for radiative heat transfer in heterogeneous granular media. *Particuology, 82*, 25–47.

Modest, M. F. (2013). *Radiative heat transfer* (3rd ed.). Elsevier.

Peng, Z., Doroodchi, E., & Moghtaderi, B. (2020). Heat transfer modelling in Discrete Element Method (DEM)-based simulations of thermal processes: Theory and model development. *Progress in Energy and Combustion Science, 79*, Article 100847.

Peters, B. (2002). Measurements and application of a discrete particle model (DPM) to simulate combustion of a packed bed of individual fuel particles. *Combustion and Flame, 131*(1–2), 132–146.

Peters, B., Baniasadi, M., & Baniasadi, M. (2018). The extended discrete element method (XDEM): An advanced approach to model blast furnace. *Iron Ores and Iron Oxide Materials, 38*(7), 1049–1054.

Peters, B., Baniasadi, M., Baniasadi, M., Besseron, X., Donoso, A. E., Mohseni, M., & Pozzetti, G. (2019). XDEM multi-physics and multi-scale simulation technology: Review of DEM–CFD coupling, methodology and engineering applications. *Particuology, 44*, 176–193.

Ranz, W. E., & Marshall, W. R. (1952). Evaporation from drops: Part II. *Chemical Engineering Progress, 48*, 173–180.

Rickelt, S., Sudbrock, F., Wirtz, S., & Scherer, V. (2013). Coupled DEM/CFD simulation of heat transfer in a generic grate system agitated by bars. *Powder Technology, 249*, 360–372.

Scherer, V., Mönnigmann, M., Berner, M. O., & Sudbrock, F. (2016). Coupled DEM–CFD simulation of drying wood chips in a rotary drum–baffle design and model reduction. *Fuel, 184*, 896–904.

Silva, J. P., Teixeira, S., Peters, B., & Teixeira, J. C. (2021). Survey of existing literature data on the biomass combustion behavior in industrial grate-fired boilers. In *ASME International mechanical Engineering congress and exposition* (Vol. 85635) American Society of Mechanical Engineers. V08AT08A008.

Spijker, C., Pollhammer, W., & Raupenstrauch, H. (2023). CFD-DEM modeling of shaft furnaces using the volume fraction smoother approach. *Chemical Engineering & Technology, 46*(7), 1333–1339.

Sudbrock, F., Kruggel-Emden, H., Wirtz, S., & Scherer, V. (2015). Convective drying of agitated silica gel and beech wood particle beds—experiments and transient DEM-CFD simulations. *Drying Technology, 33*(15–16), 1808–1820.

Tausendschön, J., Stöckl, G., & Radl, S. (2023). Machine Learning for heat radiation modeling of bi-and polydisperse particle systems including walls. *Particuology, 74*, 119–140.

Tavakkol, S., Zirwes, T., Denev, J. A., Bockhorn, H., & Stapf, D. (2023). Modeling of radiation heat transfer in dense-bed flows of solids in indirectly heated rotary kilns. *Thermal Science and Engineering Progress, 38*, Article 101545.

Vargas, W. L., & McCarthy, J. J. (2001). Heat conduction in granular materials. *AIChE Journal, 47*(5), 1052–1059.

Vargas, W. L., & McCarthy, J. J. (2002). Conductivity of granular media with stagnant interstitial fluids via thermal particle dynamics simulation. *International Journal of Heat and Mass Transfer, 45*(24), 4847–4856.

Viskanta, R., & Mengüç, M. P. (1987). Radiation heat transfer in combustion systems. *Progress in Energy and Combustion Science, 13*(2), 97–160.

Wang, Z., Teng, Y., & Liu, M. (2019). A semi-resolved CFD–DEM approach for particulate flows with kernel based approximation and Hilbert curve based searching strategy. *Journal of Computational Physics, 384*, 151–169.

Wu, H., Gui, N., Yang, X., Tu, J., & Jiang, S. (2020). Analysis and evaluations of four models of thermal radiation for densely packed granular systems. *Chemical Engineering Science, 211*, Article 115309.

https://bulk-reaction.de/. (Accessed 11 November 2024).

https://www.openfoam.com/documentation/guides/v2012/doc https://www.openfoam.com/documentation/guides/v2012/doc/(Accessed on October 12, 2024.